

An Analysis of the *Fermi* Bubbles at Low Latitudes

Bachelorarbeit aus der Physik

Vorgelegt von
Laura Herold
November 29, 2016

Erlangen Centre for Astroparticle Physics
Physikalisches Institut II
Friedrich-Alexander-Universität Erlangen-Nürnberg



Betreuer: Dr. Dmitry Malyshev,
Prof. Dr. Stefan Funk

Abstract

The *Fermi* bubbles are two large lobes of gamma-ray emission extending 55° above and below the Galactic center. This work analyses the *Fermi* bubbles at low latitudes between -10° and 10° using 8 years of data recorded by the *Fermi* Large Area Telescope. Both the longitudinal profiles of integrated intensity and the spectral energy distribution at low latitudes suggest an excess of hard emission to the right of the Galactic center. The excess remains after modelling the foreground in the Galactic plane with two different approaches: Making use of a template for the gas-correlated emission and modelling soft emission with low-energy *Fermi* data.

An excess of hard gamma-ray emission at around -5° longitude, that could be related to the *Fermi* bubbles, is further analysed. In a purely hadronic model, the gamma-ray excess could be explained by an increased cosmic-ray density of 10^{-9} GeV/cm³, created by around 880 additional supernovae. The spectrum of the excess with spectral index $n = 2.2$ is relatively hard.

Contents

1	Introduction: Gamma-ray astrophysics	7
1.1	The <i>Fermi</i> gamma-ray space telescope	7
1.2	Sources of gamma radiation	8
1.3	The <i>Fermi</i> bubbles	10
2	Searching for the origin of the Fermi bubbles in the Galactic plane	13
2.1	Longitudinal profiles at low latitudes	13
2.2	The spectral energy distribution in the vicinity of the Galactic center . . .	15
3	Modelling the foreground emission	17
3.1	Gas-model map as a template for neutral pion decay	17
3.2	Low-energy <i>Fermi</i> data as a template for soft emission	19
3.2.1	χ^2 fit of low-energy data	19
3.2.2	Maximum-likelihood fit of low-energy data and isotropic background	21
4	Analysis of an excess flux in the Galactic plane at around -5° longitude	23
4.1	Luminosity of the excess-flux region	24
4.2	Hadronic model of the emission mechanism	26
4.3	Spectral energy distribution of the excess-flux region	27
5	Summary and outlook	29
A	Appendix	31
A.1	Details about the <i>Fermi</i> -LAT data and point-sources mask	31
A.2	Calculation of intensity and SED, estimation of its statistical errors	32
A.3	The method of maximum likelihood	34
	Bibliography	37

1 Introduction: Gamma-ray astrophysics

The exploration of gamma radiation from space has opened new ways of understanding the high-energy Universe. Gamma rays are the photons with the highest energies. While the lower limit of the gamma-ray spectrum is usually defined to be at 100 keV, the highest photon energies currently observed are around 100 TeV. Since gamma radiation is absorbed by the Earth's atmosphere, it cannot be detected directly by telescopes on the ground. There are two ways to circumvent this problem as illustrated, e.g., by S. Funk [1]: Making use of the atmosphere as a detector itself or installing the detector on a satellite. Ground-based experiments detect the electromagnetic showers that are created when gamma-ray photons hit nuclei in the atmosphere. The particles in the showers create (optical) Cherenkov radiation which can be measured by telescopes on the ground.

Space-based experiments started in the mid 1960s with the satellite Explorer XI. Back then, most gamma-ray photons that were measured were created by interactions of cosmic-ray particles with the atmosphere and no individual point sources could be distinguished. Since then the resolution has increased continuously. The last generations of gamma-ray satellites, OSO-3, SAS-2, COS-B and EGRET, were already capable of detecting point sources and diffuse emission of gamma radiation inside and outside our Galaxy [1]. As published on the NASA website [3] the *Fermi* gamma-ray space telescope was launched in June 2008 (Figure 1.1), improving our opportunities of probing the high-energy Universe further.



Figure 1.1: Artists impression of *Fermi* gamma-ray space telescope [4]

1.1 The Fermi gamma-ray space telescope

There are two experiments installed on the *Fermi* gamma-ray space telescope (formerly GLAST). The Gamma-ray Burst Monitor (GBM) consists of 14 scintillators with an energy range of around 150 keV - 30 MeV for quick localization of gamma-ray bursts, extremely violent events that emit high-intensity gamma radiation. The main instrument on the satellite is the Large Area Telescope (LAT) with an energy range from 20 MeV to

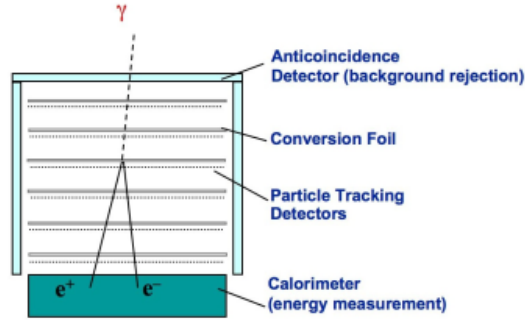


Figure 1.2: Detection mechanism for gamma-ray photons in the LAT [9]

above 300 GeV. The detection mechanism is illustrated in Figure 1.2. Gamma-ray photons hit the conversion foils, thin layers of high- Z material, and convert into electron-positron pairs. The trajectories of the secondary particles are traced by layers of particle tracking detectors, their energy is recorded by a calorimeter. The detector is surrounded by an anticoincidence shield which identifies charged particles that could be mistaken for gamma-ray photons [3].

The angular resolution of the LAT is 3.5° for 100 MeV and improves to 0.15° for energies larger than 10 GeV. The energy resolution is $< 10\%$, but worsens dramatically for energies above 300 GeV. The data recorded is publicly available and can be downloaded from NASA’s *Fermi* Science Support Center [3]. More details about the used data are given in the appendix A.1.

1.2 Sources of gamma radiation

Gamma radiation originates in non-thermal processes, i.e., there are no ‘GeV or TeV temperatures’ that could accelerate particles to high enough energies, so that they emit radiation at these high energies. Therefore, it is necessary to trace back high-energy particles to identify sources of gamma radiation. The Universe is filled with high-energy particles, called cosmic rays, which interact with the interstellar medium and radiation fields, producing gamma radiation [1]. The main contribution to the cosmic-ray population that we observe is presumably injected by supernova remnants and relativistic outflows like jets from black holes, active galactic nuclei or pulsars, which themselves emit gamma radiation. The dominant interaction mechanisms of high-energy particles are (Longair [2]):

Neutral pion decay: When high-energy protons collide with other protons, nuclei of atoms or molecules in the interstellar gas, pions (π^0, π^+, π^-) are created. The charged pions decay into muons and finally into electrons (and neutrinos), while the neutral pion almost instantly decays into two gamma-ray photons: $p + p \rightarrow \pi^0 \rightarrow \gamma\gamma$.

Inverse Compton (IC) scattering: Ultra-relativistic electrons (and positrons) can scatter low-energy photons of the interstellar radiation field to high gamma energies. The interstellar radiation field consists mainly of the cosmic microwave background, infrared radiation from dust, and starlight. Therefore, this process is stronger in star-filled regions.

Synchrotron radiation: Charged particles deflected in magnetic fields emit radiation. Since this process scales inversely with the mass of the particle, the main contribution of cosmic synchrotron radiation is produced by electrons (and positrons). This radiation is mostly emitted within the radio, optical and X-ray regime. In rare cases a contribution to the gamma regime is present. Synchrotron radiation, however, is very useful to determine whether an observed gamma signal originates in an electron-dominated process. A multi-wavelength analysis of a leptonic accelerator will show a synchrotron signal at lower energies and an IC signal at higher energies.

Bremsstrahlung: Accelerated charged particles in electric fields emit electromagnetic radiation up to the lower gamma-ray regime. Bremsstrahlung is mainly emitted by electrons (and positrons) hitting the static electric fields of atoms or molecules in the interstellar medium.

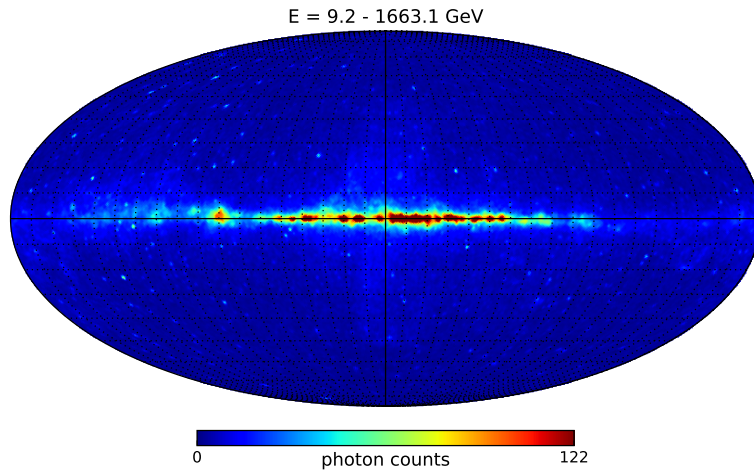


Figure 1.3: Gamma-ray photon counts map. Point sources are masked. The Fermi bubbles can be seen as two faint lobes above and below the Galactic plane. In this work all sky maps are shown in Galactic coordinates using Mollweide projection. The distance between two graticules is 10° and the center of the map coincides with the Galactic center. The energy range is specified above the map.

The gamma-ray sky shown in Figure 1.3 can be decomposed into three emission components: From every direction of the sky one measures an equal flux of gamma-ray photons. This extragalactic radiation is called **isotropic diffuse gamma-ray background**. The **diffuse emission** from the Galactic plane is far stronger than the gamma-ray background. The main contributions at these energies come from neutral pion decay, IC and bremsstrahlung. **Point sources** like supernova remnants or active galactic nuclei are not of interest in the following analysis since they overshadow the weaker diffuse emission [2]. Thus, to see large scale structures like the *Fermi* bubbles a point-sources mask is used in all maps. In the all-sky images in Galactic coordinates, like in Figure 1.3, the masked regions are filled by the average value of all neighbouring pixels. More details about the mask are given in the appendix A.1.

1.3 The Fermi bubbles

Launched in 2001, the Wilkinson Microwave Anisotropy Probe (*WMAP*) produced detailed all-sky maps of microwave radiation. Around the Galactic center a microwave haze, an excess of microwave radiation, was detected [7]. When the first measurements of the *Fermi* satellite came out, Dobler et al. [7] found a possible counterpart in the gamma-ray data, termed *Fermi* haze. After some processing by Su et al. [8] the bubble-like structure appeared.

Today, with 8 years of *Fermi* LAT data the *Fermi* bubbles, two enormous gamma-ray lobes extending 55° above and below the Galactic center, can be recognized in the pure data above 10 GeV without any further analysis (see Figure 1.3).

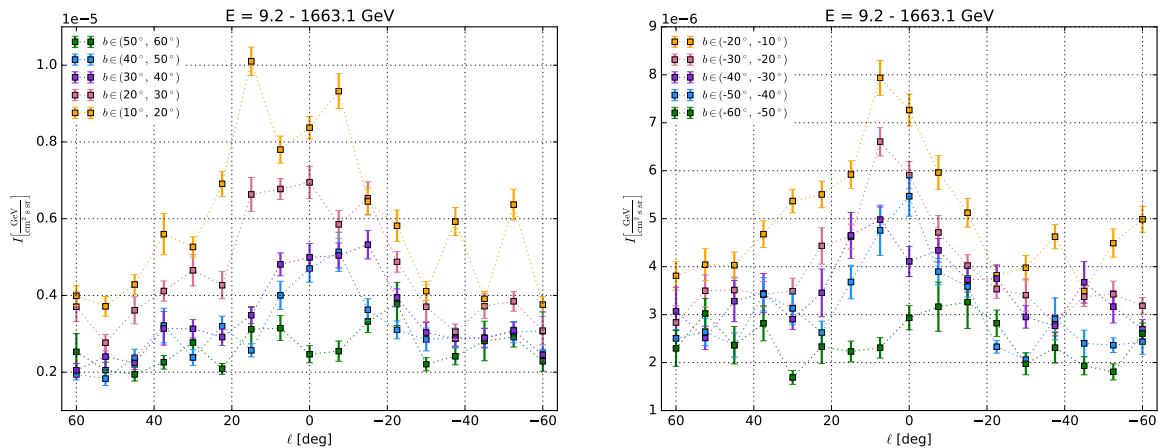


Figure 1.4: Longitudinal profiles of integrated intensity over the given energy range of the northern (left) and southern (right) hemisphere of the Galaxy. Point sources are masked. The errorbars show the statistical errors.

The shape of the gamma-ray flux created by the bubbles becomes more apparent if one analyses the data in stripes of latitude b at different longitudes ℓ , in so-called longitudinal profiles. Figure 1.4 shows the integrated intensity over 9.2 - 1663.1 GeV in $\Delta b = 10^\circ$ stripes of the northern and southern hemisphere of our Galaxy. The errorbars visualize the statistical errors. For the calculation of the mean intensity and its statistical error refer to appendix A.2. It is clearly visible that the gamma-ray emission decreases with the distance to the Galactic plane. The enhanced emission between -20° and 20° longitude is caused by the *Fermi* bubbles.

Their origin is not yet clear. Radio and X-ray lobes are common in other galaxies. Centaurus A's central black hole, for example, ejects two jets that form radio-emitting lobes as can be seen in Figure 1.5. Such lobes are often found in galaxies with large accretion onto the central supermassive black hole or with starburst activity in its neighbourhood (see discussion by Ackermann et al. [5]). Today, the Milky Way's nucleus seems inactive, but similar mechanisms might have existed before. Possible formation scenarios are: The bubbles could have been created by a jet or a spherical outflow from the supermassive black hole, by a wind from a sequence of supernova explosions, or by several shocks from accretion events onto the central black hole which must have happened a few million years ago [5]. All these mechanisms can

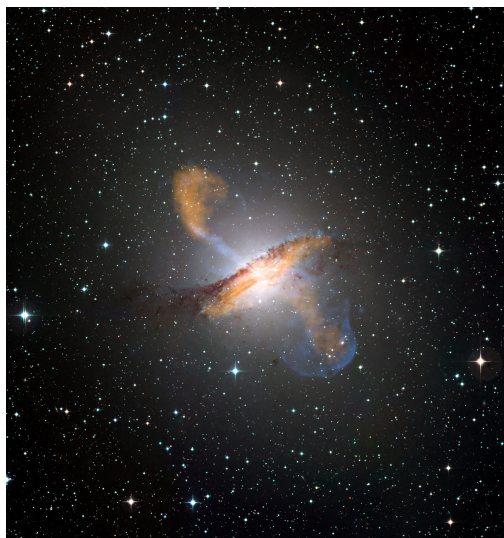


Figure 1.5: *Centaurus A*, composite image of X-ray data (blue), microwave (orange) and visible images [6]

create vast lobes that contain highly relativistic particles. Relativistic electrons or protons can emit gamma radiation via inverse Compton scattering (on the interstellar radiation field) and neutral pion decay (after collisions with cosmic rays), respectively. This would explain the gamma-ray emission we observe on earth.

No significant indication for remnants of jets in the *Fermi* bubbles could be detected so far. The sharp edges of the bubbles suggest a transient formation [5].

2 Searching for the origin of the Fermi bubbles in the Galactic plane

In order to gain more information about the origin of the *Fermi* bubbles it is crucial to determine the source of the outflow. The symmetry of the bubbles with respect to the Galactic center suggests that they originate from the supermassive black hole in the center of our Milky Way. Moreover, if the bubbles were produced by a supernova closer to earth, one would expect larger synchrotron radiation than the faint microwave haze that is observed [5].

However, the analysis at low Galactic latitudes is complicated due to the intense foreground of the Galactic plane. One hopes to ‘see’ through the foreground at high gamma-ray energies ($E > 100$ GeV) where the bubbles constitute a relatively large fraction of the total flux due to their hard spectrum. A spectrum is called hard if it does not only slowly converge against zero at high energies, i.e., the contribution at higher energies is still large.

2.1 Longitudinal profiles at low latitudes

To visualize the spatial distribution of intensity close to the Galactic plane, profile plots for $|b| < 10^\circ$ in four different energy intervals were created (see Figure 2.1). The errorbars show the statistical errors. For the calculation of the mean intensity and its statistical error consult the appendix A.2. The distance between two latitude stripes is $\Delta b = 4^\circ$. Point sources are masked and are not taken into account for the calculation of the mean intensity.

What attracts attention is the asymmetry with respect to the Galactic center. The intensity of the latitude stripe from -2° to 2° peaks at around $\ell = -10^\circ$ which is more pronounced at higher energies, indicating an extraordinary hard spectrum. The latitude stripes from -6° to -2° and from -10° to -6° show the same characteristics. It seems that there is an excess of hard emission to the right of the Galactic center, i.e., at negative longitudes.

2 Searching for the origin of the Fermi bubbles in the Galactic plane

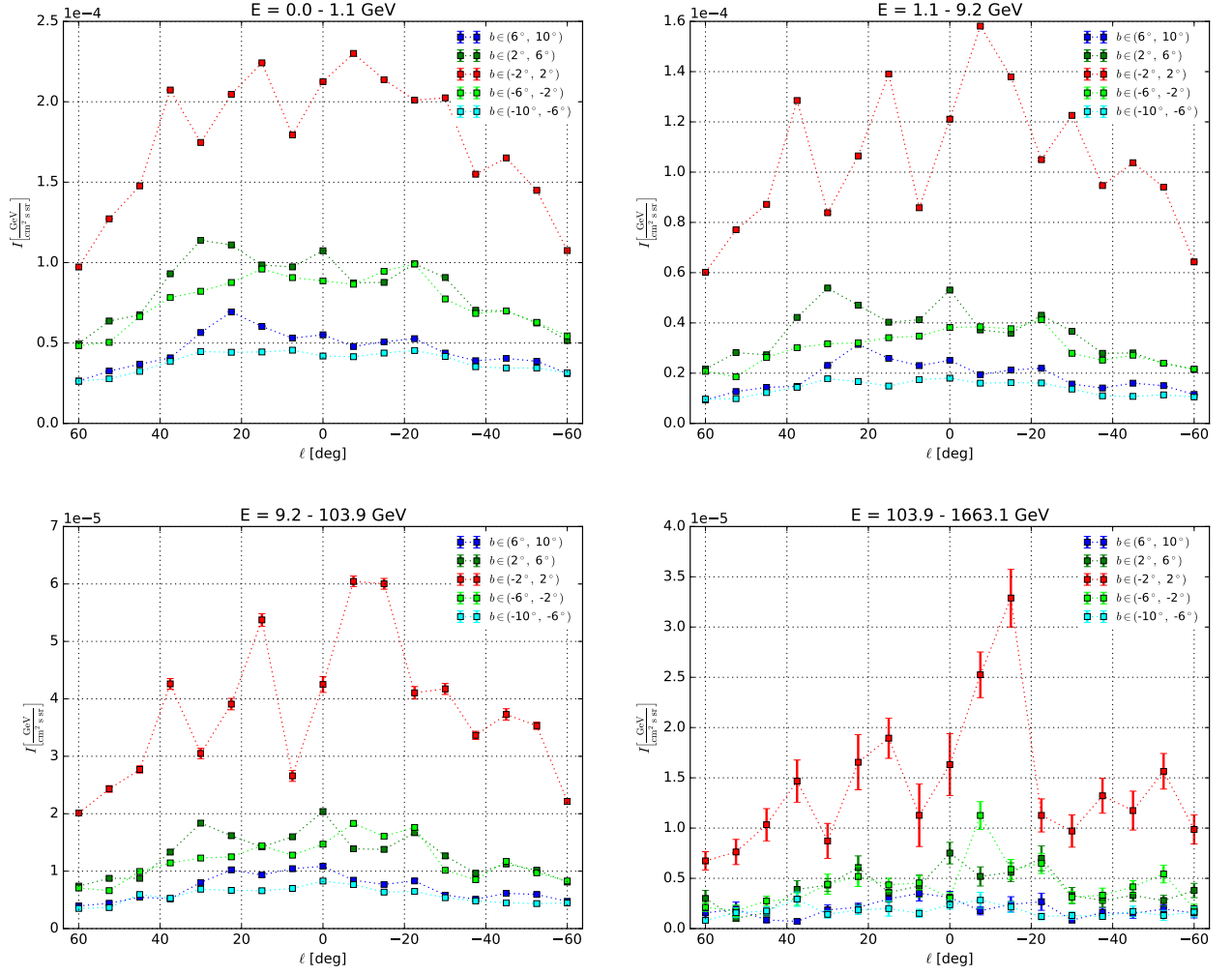


Figure 2.1: Longitudinal profiles of integrated intensity over different energy ranges. Darker colours indicate latitude stripes above the Galactic plane, lighter colours indicate latitude stripes below. The lower end of the smallest energy range is 43 MeV. Point sources are masked.

2.2 The spectral energy distribution in the vicinity of the Galactic center

To directly compare the spectrum to the right and to the left of the Galactic center, the spectral energy distribution (SED) is plotted for $\ell \in (-20^\circ, 0^\circ)$ and $\ell \in (0^\circ, 20^\circ)$ in $\Delta b = 4^\circ$ stripes, both for the southern and northern hemisphere at latitudes $|b| < 10^\circ$ (Figure 2.2). The SED is expressed in $E^2 \frac{dN}{dE}$. As the integral of the SED (over logarithmic energy scale) gives the intensity, the area under each graph is a measure for the energy content of the process.

The errorbars show the statistical errors which increase with increasing energy due to the smaller number of photons at higher energies. The calculation of the SED and its statistical errors is given in the appendix A.2.

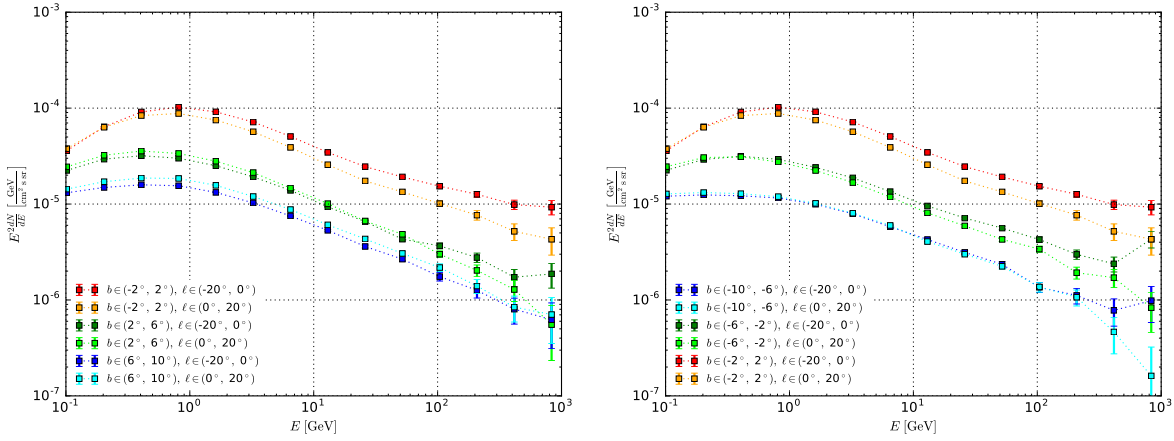


Figure 2.2: Spectral energy distribution at low latitudes. The left plot shows the SED of the north bubble, the right plot the south bubble. The graphs for $b \in (-2^\circ, 2^\circ)$ can be seen in both plots. Lighter colours indicate regions to the left, darker colours regions to the right of the Galactic center. Point sources are masked.

One observes that the SED to the right of the Galactic center, i.e., $\ell \in (-20^\circ, 0^\circ)$, is clearly harder than to the left of the Galactic center, i.e., $\ell \in (0^\circ, 20^\circ)$, at almost every latitude. This confirms that there is an excess of hard emission to right of the Galactic center.

3 Modelling the foreground emission

In order to distinguish the potential excess to the right of the Galactic center from the foreground, two methods are used. First, a gas-model map is applied to investigate if the gamma-ray excess can be explained by an excess of interstellar gas. Second, low-energy Fermi data is used as a model for soft-emission mechanisms to determine regions of extraordinary hard spectra.

3.1 Gas-model map as a template for neutral pion decay

The emission of diffuse gamma radiation is closely related to the distribution of gas. Cosmic rays colliding with the atoms and molecules of the interstellar gas emit gamma rays at GeV energies mostly via production and decay of neutral pions. Therefore, an asymmetric distribution of gas with respect to the Galactic center could explain the excess of gamma-ray emission.

Figure 3.1 (left) shows what the gamma-ray emission from collisions of cosmic rays with the interstellar gas in our Galaxy could look like. The gas-model map was calculated by the *Fermi* collaboration from *Fermi* data [14], taking into account measurements of

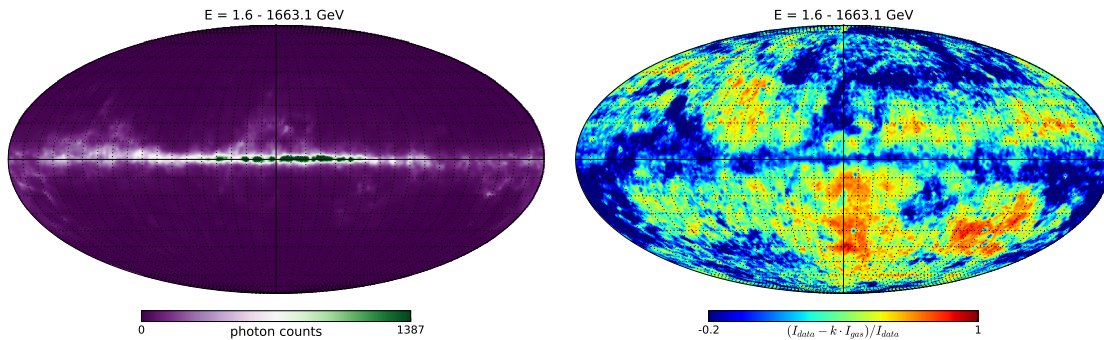


Figure 3.1: *Left: Gas model in Galactic coordinates. The map shows the number of photon counts in the given energy range produced by interactions of cosmic rays with the modelled interstellar gas distribution. Right: Residual intensity after subtraction of the gas model $k \cdot I_{gas}$ from the data I_{data} , normalized by I_{data} . The negative residuals have been suppressed for better appearance. Point sources are masked. The map is smoothed with a Gaussian of 5° FWHM.*

the 21-cm line of atomic hydrogen and the 2.6-mm line of CO, which is also a tracer of H₂. A Doppler-shift measurement of these very sharp spectral lines yields the rotational velocity of the gas particles around the Galactic center. This can be used to calculate the distribution of interstellar gas in the Milky Way. The resulting template was fitted to the data together with several other templates, e.g., for IC, bremsstrahlung, *Fermi* bubbles, sun and moon. This constrains the relative fraction of each component.

Since in this analysis only the gas-model map is used, it has to be adjusted to the scale of the data used here. Hence, the model is $I_{\text{model}} = k \cdot I_{\text{gas}}$ with the proportionality factor k . The model is fitted with the method of least squares, a χ^2 fit, to the data in each latitude stripe ℓ separately. Here $\Delta\ell = 1^\circ$ is used. k is then found from the minimization of

$$\chi_\ell^2 = \sum_b^N \frac{(\langle I_{\text{data}} \rangle_{(b,\ell)} - k_\ell \cdot \langle I_{\text{gas}} \rangle_{(b,\ell)})^2}{(\Delta \langle I_{\text{data}} \rangle_{(b,\ell)})^2}$$

with $\langle I \rangle_{(b,\ell)}$ being the mean intensity in the latitude-longitude bin (b, ℓ) of the data and gas model, respectively. For the minimization the *iminuit* package is used. The error of the model is assumed to be zero.

The residual-intensity map of the model $k \cdot I_{\text{gas}}$ subtracted from the data I_{data} and normalized by the data, is shown in Figure 3.1 (right). The Galactic plane is thoroughly covered by the model and so is the northern *Fermi* bubble. The bubble on the southern hemisphere can be recognized in the residual. Consequently, the model is not useful to isolate the bubbles from the foreground as it absorbs parts of the bubbles itself.

Nevertheless, for a closer look at the region around the Galactic center the gas-model map is applied to calculate the longitudinal profiles of integrated intensity for $|b| < 10^\circ$ in $\Delta b = 4^\circ$ stripes (Figure 3.2). Shown are both $\langle I_{\text{data}} \rangle_{(b,\ell)}$ (dotted with markers) and $\langle I_{\text{model}} \rangle_{(b,\ell)} = k_\ell \cdot \langle I_{\text{gas}} \rangle_{(b,\ell)}$ (solid). The errorbars visualize the statistical errors that are very small due to the large number of total counts in the energy range. One observes that the fit has worked well and the model traces the data roughly. For $b \in (2^\circ, 6^\circ)$ (light green) and $b \in (-6^\circ, -2^\circ)$ (green) an excess of gamma-ray emission can be seen at $\ell = 0^\circ$ and $\ell = -10^\circ$, respectively. $b \in (6^\circ, 10^\circ)$ (light blue) and $b \in (-10^\circ, -6^\circ)$ (blue) also show broad excesses around the Galactic center. For $b \in (-2^\circ, 2^\circ)$ two slight excesses might be present at $\ell = -5^\circ$ and $\ell = -15^\circ$.

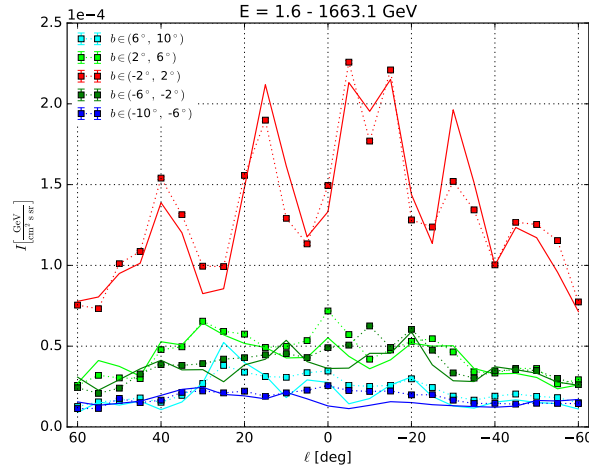


Figure 3.2: Longitudinal profiles of integrated intensity. The markers and dotted lines represent the data, the solid lines represent the gas model. Darker colours indicate latitude stripes above the Galactic plane, lighter colours indicate latitude stripes below. Point sources are masked.

3.2 Low-energy *Fermi* data as a template for soft emission

The second model of the foreground employed in this work is gained from *Fermi* data itself. Low-energy *Fermi* data can be applied as a model for the spatial distribution of comparably soft emission mechanisms like π^0 decay, which dominates over the other emission mechanisms in the relevant energy range. This technique has been used by Dobler et al. [7] to make the *Fermi* haze visible in the first place. Its great advantage is that no further modelling assumptions are necessary.

3.2.1 χ^2 fit of low-energy data

Like in the case of the gas model a χ^2 fit is employed to determine the proportionality factor k of the model $I_{\text{model}} = k \cdot I_{\text{low}}$. For the integrated intensity I_{low} that is used for the model, 43 MeV - 1.6 GeV has proven to be a suitable energy interval. I_{high} denotes the integrated intensity over the higher energy interval, i.e., the data, which is 1.6 GeV - 1.7 TeV in the following.

Figure 3.3 shows the residual-intensity map after subtraction of the model, i.e., high residual intensity marks regions of hard emission spectra. The *Fermi* bubbles are clearly visible as two lobes with extraordinary hard spectra. Point sources have not been masked in this map since the difference in the resulting residual-intensity maps is only small. Including the point sources reveals one general problem of the modelling technique: The point spread function at lower energies is wider than at higher energies. This correlation

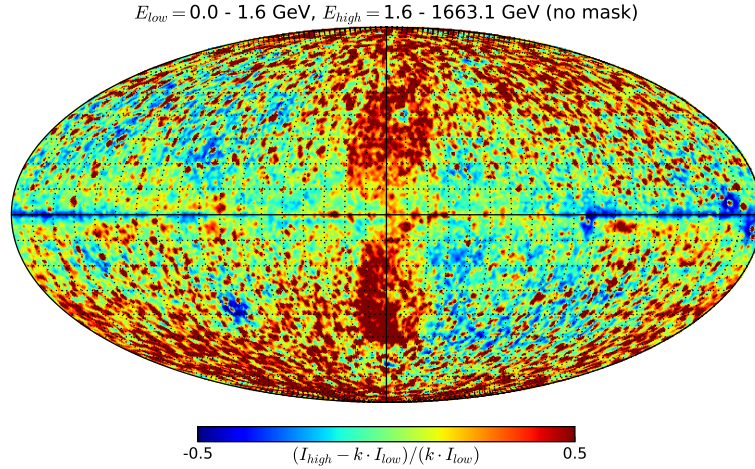


Figure 3.3: Residual-intensity map after subtraction of the model created by low-energy *Fermi* data, normalized by the model. The parameters have been determined by a χ^2 fit. No point-sources mask is used. The map is smoothed with a Gaussian of 5° FWHM.

has its origin in the reconstruction of the photon’s incident angle in the detector. The determination of the direction of a low-energy gamma-ray photon is less reliable than that of a high-energy photon. This is nicely demonstrated by the negative hole in the upper part of the northern bubble. In the middle of the hole a point source can be detected. According to the *Fermi* Science Support Center [3] the point source is PKS 1510-08¹, a flat spectrum radio quasar (FSRQ). The emission in the lower-energy range is spread over a wide disk while the higher-energy range is centered in one spot. As the model consists of low-energy data this wide circle shows in the residual as a large hole. Furthermore, the point-sources mask cannot fix the problem because it covers only a small spot in the center of the disk. For more details on the mask, see the appendix A.1.

In total, this simple model is sufficient to determine the shape of the bubbles very precisely. The residual (Fig. 3.3) gives the impression that the *Fermi* bubbles originate not from the Galactic center but from a region to the right of it.

¹http://fermi.gsfc.nasa.gov/ssc/data/access/lat/4yr_catalog/3FGL-table/

3.2.2 Maximum-likelihood fit of low-energy data and isotropic background

Unfortunately, the χ^2 -fitting procedure encounters a problem if the number of counts in one bin is zero. Therefore, a **likelihood** fit is applied to improve the performance. Since the approach to use low-energy *Fermi* data seems promising, this method is kept to model the soft emission in our Galaxy. Additionally, the model is improved by another parameter c that takes the isotropic gamma-ray background into account. The total model $N_{\text{model}} = k \cdot N_{\text{low}} + c$ is again fitted in 1° -latitude stripes to the data N_{high} . Since for the method of maximum likelihood a Poisson-distributed variable is required, instead of the integrated intensity one uses the number of photon counts in each latitude-longitude bin and each energy interval. In order to reduce the formation of holes by point sources in the residual, the lower energy interval is set to 600 MeV - 1.6 GeV. This time the region of the bubbles, i.e., $\ell \in (-20^\circ, 20^\circ)$, is excluded from the fit to avoid an over-compensation of the hard emission by the model. Point sources are masked. For details on the likelihood fit see the appendix A.3.

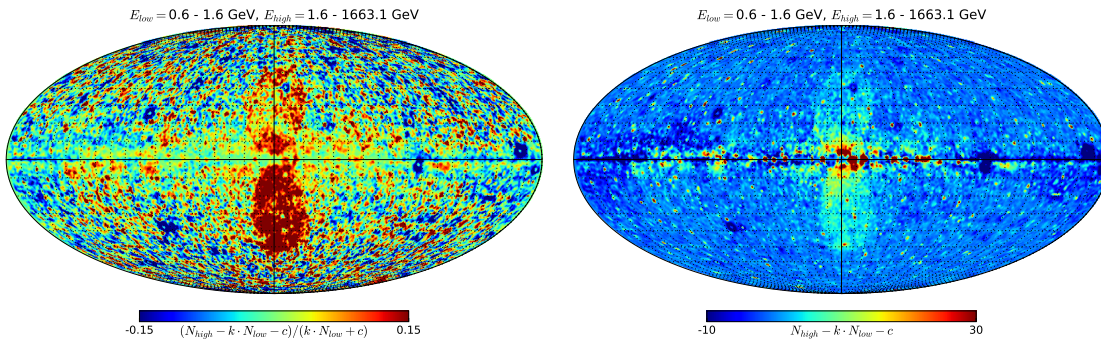


Figure 3.4: Residual photon-counts map after subtraction of the model, normalized (left) and not normalized by the model (right). The energy range of the model is given by E_{high} , the energy range of the data by E_{low} . The map is smoothed with a Gaussian of 5° FWHM. Point sources are masked.

The resulting residual photon-counts map is shown in Figure 3.4. The *Fermi* bubbles are again clearly visible. In the left map of Figure 3.4 the residual has been normalized by the model, revealing the bubbles again as two lobes of hard spectra. The right map of Figure 3.4 shows the total residual photon counts, making regions of high-excess emission visible. One excess to the right of the Galactic center in the Galactic plane at $\ell = -5^\circ$ attracts attention. It seems to be connected to the bubbles by a band of hard emission. Further to the right another excess emission stands out at $\ell = -15^\circ$. The Galactic center itself appears to have a comparatively soft spectrum.

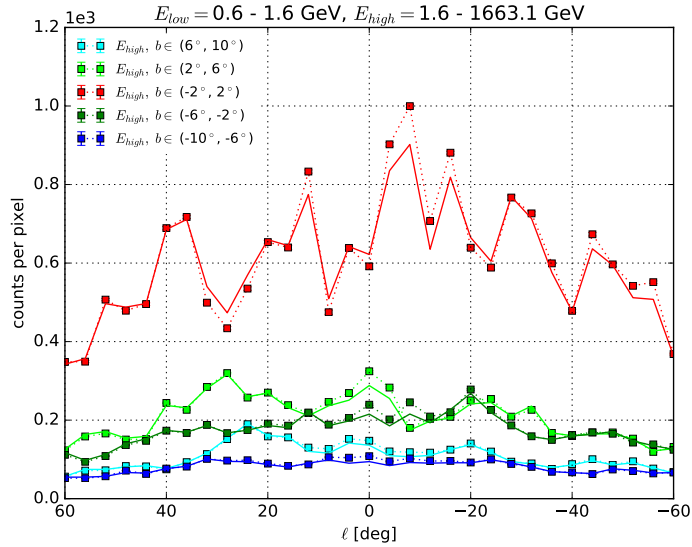


Figure 3.5: Longitudinal profiles of photon counts per pixel at small latitudes. Darker colours indicate latitude stripes above the Galactic plane, lighter colours indicate latitude stripes below. The region of the bubbles, i.e., $\ell \in (-20^\circ, 20^\circ)$, is excluded from the fit. Point sources are masked.

In Figure 3.5 the model is further analyzed at low latitudes. Shown are the longitudinal profiles of photon counts at $|b| < 10^\circ$ in $\Delta b = 4^\circ$ stripes. The two excesses that were discovered in the all-sky map are again visible at $b \in (-2^\circ, 2^\circ)$, and $\ell = -5^\circ$ and $\ell = -15^\circ$, respectively. The two stripes below the Galactic plane, i.e., $b \in (10^\circ, -2^\circ)$, indicated by darker colours, show both an excess at the Galactic center and one at around $\ell = -8^\circ$ to the right of the Galactic center. On the other hand, the two stripes above the Galactic plane, i.e., $b \in (2^\circ, 10^\circ)$, indicated by lighter colours, possess excessive hard emission centered around the Galactic center.

Accordingly, all modelling done in this work indicates an asymmetry with respect to the Galactic center. Hard gamma radiation seems to be more abundant to the right of the Galactic center. Since the spectrum of the *Fermi* bubbles themselves is very hard, it is reasonable to look out for regions of extraordinary hard spectra in the Galactic plane. They might be related to the origin of the *Fermi* bubbles.

4 Analysis of an excess flux in the Galactic plane at around -5° longitude

One excess in the Galactic plane, found in section 3.2.2, seems to be particularly interesting. To the right of the Galactic center at around -5° longitude in the Galactic plane an ellipsoidal excess region appeared to be connected to the *Fermi* bubbles by a band of extraordinary hard emission. This section concentrates on the characteristics of this very excess region, marked in Figure 4.1 by a red rectangle, from now on called ‘region of interest’ (ROI).

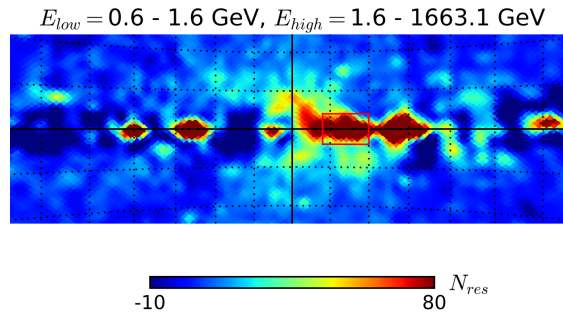


Figure 4.1: Close-up view of the residual photon-counts map (plotted with *healpy*’s *gnomview*). Low-energy *Fermi* data and isotropic background is used as a model, i.e., $N_{res} = N_{high} - k \cdot N_{low} - c$. The center of the map coincides with the Galactic center. The red region indicates the excess of hard gamma-ray emission. The distance between two graticules is 5° . The map is smoothed with a Gaussian of 5° FWHM. Point sources are masked.

The model applied in this section, is the one defined in section 3.2.2, i.e., low-energy *Fermi* data and isotropic background. The residual counts are therefore given by $N_{res} = N_{high} - k \cdot N_{low} - c$.

4.1 Luminosity of the excess-flux region

One fundamental information we can gain from *Fermi* data about the ROI is its luminosity. The luminosity is defined as the total amount of energy emitted by the ROI per unit time. In terms of intensity the luminosity per unit area can be written as

$$\frac{dL}{dA} = \int_{\text{ROI}} I_{\text{tot}}(E_0, \Omega) d\Omega. \quad (4.1)$$

Intensity in this section denotes the **residual** intensity, as we are interested in excessive radiation from the ROI that is not contained in the model.

Since the sensitivity of the *Fermi* LAT has a limited range, we cannot observe the full spectrum of the ROI. Additionally, 600 MeV - 1.6 GeV are used as a model and cannot be taken into account for the residual emission. As the upper end of the sensitivity spectrum is rather high, it can be set to infinity. Therefore, the total intensity is given by

$$I_{\text{tot}}(E_0, \Omega) = \int_{E_0}^{\infty} I(E, \Omega) dE \quad (4.2)$$

with $E_0 = 1.6$ GeV being the lower end of the spectrum. Using the expression of the intensity described in appendix A.2 one gets

$$\frac{dL}{dA} = \int_{\text{ROI}} \int_{E_0}^{\infty} E \frac{dN^\gamma}{d\Omega dE \tau} dE d\Omega \approx \sum_{i \in \text{ROI}} \sum_{j: E_j > E_0} E_j \frac{N_{ij}^\gamma}{\tau_{ij}} \quad (4.3)$$

where E_j is the mean energy of energy bin j , N_{ij}^γ and τ_{ij} are the number of photon counts and exposure in pixel i and energy bin j , respectively.

The edges of the ROI are determined by eye. This calculation adds all pixels for $b \in (-2^\circ, 2^\circ)$ and $\ell \in (-10^\circ, -4^\circ)$ to the ROI. The borders of the ROI are indicated in Figure 4.1 by a red rectangle.

For this choice of coordinates, the luminosity from the ROI per unit detector area is approximately

$$\frac{dL}{dA} = 2.9 \cdot 10^{-10} \frac{\text{erg}}{\text{cm}^2 \text{s}}. \quad (4.4)$$

Assuming that the ROI is close to the Galactic center, as it would be expected if it was related to the *Fermi* bubbles, the total luminosity of the ROI is

$$L = \int_{\text{Sphere with radius } R} \frac{dL}{dA} dA = 4\pi R^2 \frac{dL}{dA} = 2.2 \cdot 10^{36} \frac{\text{erg}}{\text{s}} \quad (4.5)$$

with the distance $R = 8$ kpc to the ROI. Expressed in solar luminosities the luminosity becomes $L = 572 L_\odot$, or expressed in terms of luminosity per area from the Crab nebula $\frac{dL}{dA} = 12$ mCrab. Since both emitters radiate in a different energy range than the ROI,

a comparison only makes limited sense. While the sun mainly emits in the ultraviolet, optical and infrared regime, the Crab nebula is commonly used as a X-ray standard candle in the energy range from 2 to 10 keV, where it has a total luminosity per area of $\frac{dL}{dA} = 2.4 \cdot 10^{-8} \frac{\text{erg}}{\text{cm}^2\text{s}}$ [10].

4.2 Hadronic model of the emission mechanism

In order to learn more about the emission mechanisms that could create an excess of hard emission like the one we observe from the ROI, one needs to make assumptions. Let's assume for now that the excessive gamma-ray emission is produced by neutral pion decay **only**. How much additional cosmic radiation would be needed to explain the residual gamma radiation from the ROI? (Values and certain formulas are taken from [2].)

To calculate the cosmic-ray density ρ_{CR} , we assume the gas density in the ROI to have a typical value for the inner Galaxy, i.e., $\rho_{\text{gas}} = \frac{1}{\text{cm}^3}$. Since cosmic rays are highly relativistic we can approximate their velocity by the speed of light, $v_{\text{CR}} = c$. The proton-proton cross section $\sigma_{\text{pp}} = 2.5 \cdot 10^{-26} \text{ cm}^2$ for pion production is similar to the geometric size of the proton.

Then, the average number of collisions per unit time and area is $P_{\text{col}} = \rho_{\text{gas}} \sigma_{\text{pp}} \rho_{\text{CR}} v_{\text{CR}}$. However, collisions between cosmic-ray protons and protons or nuclei of the interstellar gas produce not only π^0 mesons, but also π^+ and π^- mesons. The charged pions decay into muons and further into electrons (and neutrinos). Though, leptons can emit gamma radiation via inverse Compton scattering, this is not taken into account in this calculation. Only the neutral pion decays into two gamma-ray photons. Therefore, only one third of the energy in cosmic rays is converted into gamma radiation. This is expressed in the energy branching ratio $F(E_{\text{CR}}, E_\gamma)$, with $\int F(E_{\text{CR}}, E_\gamma) dE_\gamma = \frac{1}{3} E_{\text{CR}}$. With that, the luminosity of the ROI can also be written in terms of P_{col} :

$$\begin{aligned} \frac{dL}{dV} &= \int P_{\text{col}}(E_{\text{CR}}) \int F(E_{\text{CR}}, E_\gamma) dE_\gamma dE_{\text{CR}} \\ &= \frac{1}{3} \rho_{\text{gas}} \sigma_{\text{pp}} \int \rho_{\text{CR}} v_{\text{CR}} E_{\text{CR}} dE_{\text{CR}} \\ &= \frac{1}{3} \rho_{\text{gas}} \sigma_{\text{pp}} c \epsilon_{\text{CR}} \end{aligned} \quad (4.6)$$

where $\epsilon_{\text{CR}} = \int \rho_{\text{CR}} E_{\text{CR}} dE_{\text{CR}}$ is the energy density of cosmic radiation.

With the value of the total luminosity L that was calculated in the previous section, one gets for the cosmic-ray energy density:

$$\epsilon_{\text{CR}} = \frac{3}{\rho_{\text{gas}} \sigma_{\text{pp}} c} \frac{L}{V_{\text{ROI}}} = 8.8 \cdot 10^{51} \frac{\text{erg}}{V_{\text{ROI}}} = 1.5 \cdot 10^{-12} \frac{\text{erg}}{\text{cm}^3}. \quad (4.7)$$

Thereby, the luminosity L is assumed to be constant over the volume V_{ROI} of the ROI. The volume V_{ROI} is assumed to have an ellipsoidal shape. The length and height was set to the length and height of the rectangle that is marked in Figure 4.1 with red lines, assuming a distance of 8 kpc between the ROI and earth. The depth of the ROI is assumed to be the same as the length. This yields the following volume of the ROI:

$$V_{\text{ROI}} = \frac{4}{3} \pi \cdot 279 \text{ pc} \cdot (418 \text{ pc})^2 = 0.20 \text{ kpc}^3. \quad (4.8)$$

The average energy release of a supernova in cosmic radiation is approximately $E_{\text{SNR}} \approx 10^{49}$ erg. Hence, the cosmic-ray density necessary for the observed luminosity could be explained by around **880 supernovae**.

Assuming an average supernova rate of $\frac{1}{\text{century}}$ in our galaxy, a rough estimate for the supernova rate in a region like the ROI could be $\frac{1}{\text{kyr}}$. Therefore, the timescale in which the ROI has formed, is around 1 Myr. Interestingly, this coincides with the cooling time of the electrons in the *Fermi* bubbles within the leptonic model of Ackermann et al. [5].

Another question one could ask is: What would be the distance of the excess when the additional cosmic-ray density was created by one supernova? To answer that question we rearrange Equation 4.5 and put in Equation 4.4 and 4.7. We get

$$R_{\text{1SN}} = \sqrt{\frac{L}{4 \pi \frac{dL}{dA}}} = \sqrt{\frac{\rho_{\text{gas}} \sigma_{\text{pp}} c E_{\text{SNR}}}{12 \pi \frac{dL}{dA}}} = \sqrt{\frac{1}{880}} \cdot 8 \text{ kpc} = 270 \text{ pc} \quad (4.9)$$

which is a reasonable distance. Hence, the excess could also be explained by a close-by supernova remnant.

4.3 Spectral energy distribution of the excess-flux region

Besides the luminosity, also the spectral energy distribution sheds light on the emission mechanism in a gamma-ray source. Figure 4.2 (top) shows the SED of both the data and the model. To construct the model, low-energy *Fermi* data and isotropic background (see section 3.2.2) are used. Figure 4.2 (bottom) shows the resulting residual SED. The errorbars indicate the statistical uncertainties. One observes that only at the highest energy the SED of the data lies below the SED of the model. In the logarithmic plot, the corresponding point of the residual is negative and, therefore, only its errorbar can be seen.

To determine the spectral index n , a power law

$$\frac{dN}{dE} = N_0 \left(\frac{E}{E_0} \right)^{-n} \quad (4.10)$$

is fitted to the residual data with the method of least squares, already described in section 3.1. N_0 denotes the number of photon counts at energy E_0 which can be freely chosen. The first and last points have not been taken into account for the fit, as the first point at 1.9 GeV is still strongly influenced by the model that contains *Fermi* data below 1.6 GeV, and the last point is negative.

The fit yields a spectral index of $n = 2 + \gamma = 2.18$, where γ denotes the spectral

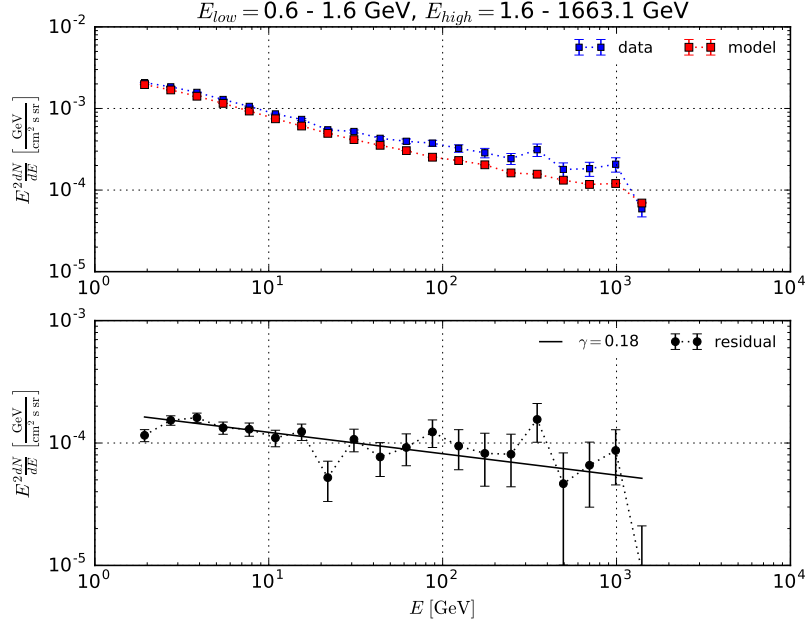


Figure 4.2: Spectral energy distribution of the ROI. Top: SED of data (blue) and model (red). The energy range of the data is specified by E_{high} , the energy range of the model by E_{low} . Bottom: Residual SED (data - model). A power law has been fitted to the residual data, the spectral index is $n = 2 + \gamma = 2.18$. The first and last points have not been taken into account for the fit. Point sources are masked.

index of $E^2 \frac{dN}{dE}$. Typical spectral indices are, for example, $n = 2.4$ for IC and $n = 2.6 - 2.7$ for neutral pion decay. The observed spectrum is much harder.

Moreover, the χ^2 fit is mainly dominated by the points below 10 GeV that have very small statistical errors. If one takes a closer look at the points between 20 GeV and 1 TeV, the spectrum seems to be almost flat, i.e., $n \approx 2.0$. Since one could argue that the points below 10 GeV are still very close to the energy range of the model, i.e., 43 MeV - 1.6 GeV, the actual spectrum of the ROI could be closer to $n \approx 2.0$ than the fit would suggest. There is no apparent explanation for such a hard spectrum.

5 Summary and outlook

The aim of this work was to separate the *Fermi* bubbles from the foreground of the Galactic plane. With this in mind, photon counts were averaged over different regions and different energy ranges. The most meaningful of these calculations are shown in **section 2**. Both the longitudinal profiles (Fig. 2.1) and the spectrum (Fig. 2.2) indicate regions of hard spectra, preferably to the right of the Galactic center.

To have a closer look at these regions and possibly find explanations for the hard gamma-ray emission, two approaches are used to model softer emission from the Galactic plane in **section 3**. Using the gas-model map as a template is reasonable since the emission in this energy range is dominated by neutral pion decay, but for further analyses one should use the template for IC and bremsstrahlung simultaneously. Low-energy *Fermi* data proved to be a suitable model for diffuse emission in the Galactic plane. An additional isotropic-background component improved the result. Therefore, the model was used in all following calculations.

With the help of this model the outline of the *Fermi* bubbles could be traced very precisely in all-sky maps (Fig. 3.4) and interesting regions could be identified in profile plots (Fig. 3.5). A recurring result was excessive hard gamma-ray emission from the right of the Galactic center, most prominently at $\ell = -5^\circ$ and $\ell = -15^\circ$.

If the base of the bubbles happens to be not the Galactic center, many of the formation scenarios stated in section 1 are disfavored. More sophisticated analyses have also found excesses of gamma radiation off the Galactic center. Acero et al.'s [16] residual all-sky map, that can be seen in Figure 5.1, shows an excess between $\ell = -10^\circ$ and $\ell = 0^\circ$. Their so-called 'baseline interstellar model' contains templates for gas-correlated emission, IC, isotropic background, earth limb intensities, sun, moon and point sources.

Section 4 concentrates on the excess at $\ell = -5^\circ$ which seems to be connected to the bubbles by a band of hard emission. The luminosity of the excess is $2.2 \cdot 10^{36} \frac{\text{erg}}{\text{s}}$, assuming a distance of $R = 8$ kpc. Such a luminosity could be explained in a purely hadronic model by the injection of cosmic rays from approximately 880 supernovae. The SED of the ROI seen in Figure 4.2 shows a hard spectrum with a spectral index $n = 2.18$. Since the ROI emits a hard and high-intensity spectrum, it may be possible to detect it, for example, with H.E.S.S. (High Energy Stereoscopic System¹), a system of Imaging

¹<https://www.mpi-hd.mpg.de/hfm/HESS/>

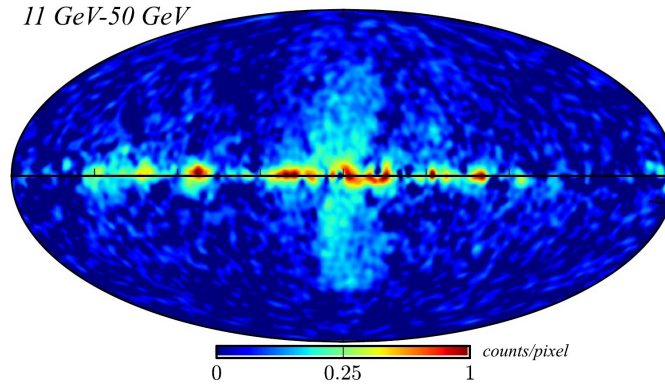


Figure 5.1: *Residual after subtraction of the ‘baseline interstellar model’ from the data. Two graticules in the horizontal are 45° apart [16]*

Atmospheric Cherenkov Telescopes with an energy range of around 10 GeV to 10 TeV. Moreover, if the gamma-ray flux is produced in a hadronic process, there should be a neutrino counterpart that could be searched for with current and future neutrino observatories.

Thus, further investigations of the models and the resulting residuals in search of emission related to the *Fermi* bubbles would be interesting. A possible extension of this analysis could contain the following projects:

- The gas model in section 3.1 should be used simultaneously with the models for IC and bremsstrahlung from [14].
- One could estimate the electron density that would be necessary to create the observed excess flux via IC only.
- The spectra of the protons and electrons in the ROI could be derived.
- Within a multiwavelength analysis, one could search for a counterpart of the gamma-ray excess in microwave or infrared data.
- It would be interesting to check if there is an excess of supernova remnants and/or X-ray binary systems in that area.

A Appendix

A.1 Details about the Fermi-LAT data and point-sources mask

Fermi LAT data is stored in FITS (Flexible Image Transport System) files. This is a standard format for data storage in astrophysics. The data¹ is publicly available and can be downloaded from the *Fermi* Science Support Center [3].

This analysis is done with 8 years (August 4, 2008 - August 3, 2016) of LAT data using standard good-time intervals, i.e., excluding for example calibration runs. Only events from a zenith angle $< 100^\circ$ are taken into account.

Since in this work statistics, i.e., a high number of counts, is more important than the purity of the signal, the Source class is used. Figure A.1 shows why: The effective area as a function of energy depends strongly on the event class. The effective area is the physical area of the satellite modified by the detection efficiency at a certain energy in a certain angle (here: on-axis). Therefore, it is a measure for the number of photons that can be detected at a certain energy.

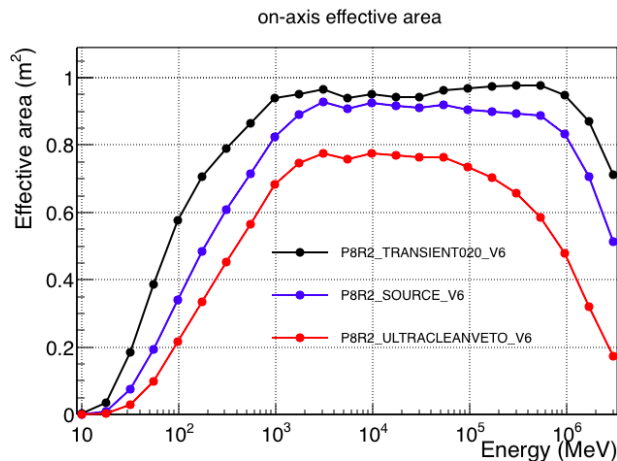


Figure A.1: Effective area of different event classes as a function of energy (on-axis). The effective area of the Source class, that is used in this work, is considerably larger than that of the UltraCleanVeto class, especially at higher energies [15].

¹<http://fermi.gsfc.nasa.gov/ssc/data/access/>

Though, the UltraCleanVeto class provides a better protection against the misclassification of charged particles as gamma rays, the effective area is smaller than for the Source class and decreases rapidly at higher energies. As particularly high-energy photons are of interest in this work, the Source class was selected.

The maps are organized in HEALPix format (Hierarchical Equal Area isoLatitude Pixelization of a sphere) which divides the surface of a sphere (here: the sky) in pixels of the same size. In this case the number of pixels is $n_{\text{pix}} = 196608$. More details are given on the HEALPix website [13].

The total energy range from 42.7 MeV to 1.66 TeV is covered by $n_{\text{energies}} = 31$ energy bins with equal logarithmic distance $\Delta \approx 0.35$.

A *Fermi*-LAT FITS file is organized in three HDUs (header data units). HDU[0] contains general information, while HDU[1] stores the measured photon counts in a $n_{\text{pix}} \times n_{\text{energies}}$ matrix. HDU[2] is an array with n_{energies} entries which contains the corresponding geometric mean E_j of the energy bin j . Therefore, the width of the energy bin j is

$$\Delta E_j = E_{j,\text{max}} - E_{j,\text{min}} = e^{\frac{\Delta}{2}} E_j - e^{-\frac{\Delta}{2}} E_j = 2 \sinh\left(\frac{\Delta}{2}\right) E_j \approx 0.35 E_j$$

The **point-sources mask** that is used in most calculations covers the 200 brightest gamma-ray sources of the 2FGL (second *Fermi* Gamma-ray LAT) catalog² by a circle of radius $\frac{\delta}{\sqrt{2}} + 1^\circ$ with δ being the angle spanned by the sidelength of one pixel. In the Mollweide projections, the masked regions are filled with the average photon-count value of all neighbouring pixels.

A.2 Calculation of intensity and SED, estimation of its statistical errors

In this work, **intensity** is defined as the power per effective detector area and per solid angle of the sky. In terms of the accessible quantities that are measured by the satellite the intensity I_i in pixel i of the sky map can be reformulated as

$$\begin{aligned} I_i &= \frac{\text{power in given energy interval detected in pixel } i}{\text{effective detection area} \times \text{solid angle per pixel}} \\ &= \frac{\text{total photon energy in given energy interval detected in pixel } i}{\text{observation time} \times \text{effective detection area} \times \text{solid angle per pixel}} \end{aligned} \quad (\text{A.1})$$

Thereby, the effective detection area of the satellite is the physical area of the satellite modified by the detection efficiency at a certain energy in a certain angle. The ‘observation time \times the effective detection area’ is defined as a new quantity called **exposure**. As the

²http://fermi.gsfc.nasa.gov/ssc/data/access/lat/2yr_catalog/

effective detection area depends on energy the exposure $\tau_i(E)$ in pixel i is also a function of energy E .

The solid angle per pixel is constant and given by $\Delta\Omega = \frac{4\pi}{n_{\text{pix}}} \approx 6.4 \cdot 10^{-5}$ sr, where the total number of pixels in the sky map is $n_{\text{pix}} = 196608$.

Therefore, the total integrated intensity over the energy range $(E_{\text{min}}, E_{\text{max}})$ in pixel i is

$$\begin{aligned}
 I_i &= \int_{E_{\text{min}}}^{E_{\text{max}}} E \frac{dN_i(E)}{dE} dE = \int_{E_{\text{min}}}^{E_{\text{max}}} E \frac{dN_i^\gamma(E)}{d\tau(E) d\Omega dE} dE \\
 &\approx \sum_{j: E_j \in (E_{\text{min}}, E_{\text{max}})} E_j \frac{N_{ij}^\gamma}{\tau_{ij} \Delta\Omega}.
 \end{aligned} \tag{A.2}$$

with $\frac{dN_i(E)}{dE} = \frac{dN_i^\gamma(E)}{d\tau(E) d\Omega dE}$ being the number of photon counts detected in pixel i per exposure, solid angle and energy. $N_i(E)$ thus already denotes the particle flux from a certain direction $d\Omega$, whereas $N_i^\gamma(E)$ is the raw number of detected photon counts in i that is stored in the FITS files.

Since we are dealing with binned data, a given photon belongs to a certain energy range. We approximate the energy of a photon in energy bin j by the mean energy E_j . N_{ij}^γ and τ_{ij} are the number of photon counts and exposure in pixel i and energy bin j , respectively.

In most applications the intensity is also binned in space. In galactic coordinates it makes sense to group pixels in latitude-longitude (lat-lon) bins (b, ℓ) . b and ℓ can be imagined as the coordinate pointing to the middle of the ‘rectangular’ lat-lon bin (b, ℓ) , the side length of the bins can have any value. The mean intensity in the lat-lon bin (b, ℓ) is

$$\langle I \rangle_{(b, \ell)} = \sum_{i \in (b, \ell)} \frac{I_i}{n_{\text{pix}(b, \ell)}} = \frac{1}{n_{\text{pix}(b, \ell)}} \sum_j \sum_{i \in (b, \ell)} E_j \frac{N_{ij}^\gamma}{\tau_{ij} \Delta\Omega} = \sum_j \langle I \rangle_{(b, \ell)j}, \tag{A.3}$$

where $\langle I \rangle_{(b, \ell)j}$ denotes the mean intensity in the lat-lon bin (b, ℓ) and energy bin j . $\langle I \rangle_{(b, \ell)}$ is in this work just referred to as I . j is always running over all energy bins in the desired energy range and $n_{\text{pix}(b, \ell)}$ is the number of pixels in the lat-lon bin.

While the systematic errors are too complicated to be taken into account, the statistical error on the mean intensity in one lat-lon bin can be estimated. The first step is to determine the standard deviation of the photon counts per pixel. The number of counts N_{ij}^γ per pixel i and energy bin j follow the **Poisson distribution**. This can be justified by the following reasoning:

If one considers all the regions along the line of sight of one single pixel that could emit a photon in the direction of the satellite with the same probability, the probability to observe a certain number of photons from all regions is binomial distributed. In the limit of a large number of regions and a small probability for one region to emit a photon, the binomial distribution can be approximated by the Poisson distribution. (Alternatively,

one could imagine one pixel to consist of a large number of subpixels.) Therefore, assuming a Poisson distribution, the standard deviation is

$$\Delta N_{ij}^\gamma = \sqrt{N_{ij}^\gamma} \quad (\text{A.4})$$

Using error propagation, the variance of the intensity is

$$\begin{aligned} (\Delta \langle I \rangle_{(b,\ell)})^2 &= \sum_j \sum_{i \in (b,\ell)} \left(\frac{\partial \langle I \rangle_{(b,\ell)}}{\partial N_{ij}^\gamma} \right)^2 \cdot (\Delta N_{ij}^\gamma)^2 \\ &\approx \sum_j \left(\frac{E_j}{\langle \tau \rangle_j \Delta \Omega n_{\text{pix}(b,\ell)}} \right)^2 \sum_{i \in (b,\ell)} N_{ij}^\gamma \end{aligned} \quad (\text{A.5})$$

and the standard deviation

$$\Delta \langle I \rangle_{(b,\ell)} = \sqrt{\sum_j \frac{(\langle I \rangle_{(b,\ell)j})^2}{N_{(b,\ell)j}^\gamma}}. \quad (\text{A.6})$$

with $N_{(b,\ell)j}^\gamma$ being the total number of photon counts in the lat-lon bin (b, ℓ) and energy bin j . This is valid since the exposure τ does vary only slightly in one lat-lon bin and can be replaced by its mean $\langle \tau \rangle_j$. The error on the exposure is assumed to be zero.

The **spectral energy distribution (SED)** in pixel i and energy bin j can be calculated from the data via

$$\left(E^2 \frac{dN}{dE} \right)_{ij} \approx E_j^2 \frac{N_{ij}^\gamma}{\tau_{ij} \Delta \Omega \Delta E_j} \quad (\text{A.7})$$

and thus the mean SED in one lat-lon bin is

$$\left\langle E^2 \frac{dN}{dE} \right\rangle_{(b,\ell)j} \approx \frac{E_j^2}{\Delta \Omega \Delta E_j} \sum_{i \in (b,\ell)} \frac{N_{ij}^\gamma}{\tau_{ij}}. \quad (\text{A.8})$$

The statistical error on the SED can be estimated in a similar way as for the intensity and is given by

$$\Delta \left\langle E^2 \frac{dN}{dE} \right\rangle_{(b,\ell)j} \approx \frac{1}{\sqrt{N_{(b,\ell)j}^\gamma}} \cdot \left\langle E^2 \frac{dN}{dE} \right\rangle_{(b,\ell)j}. \quad (\text{A.9})$$

A.3 The method of maximum likelihood

In order to fit a model of gamma-ray emission to data that possibly contains empty latitude-longitude bins, i.e., bins with no counts, a χ^2 fit is biased. For the χ^2 fit, empty bins were set to a sufficiently small number (10^{-30}).

The alternative is the maximum-likelihood fit, nicely explained by G. Cowan [11]. Since the likelihood-fit requires Poisson-distributed variables, we cannot fit the intensities directly (like for the χ^2 fit) but need to fit the photon counts. The number of counts in pixel i is a Poisson-random variable:

$$f(N_i, \mu_i) = \frac{\mu_i^{N_i}}{N_i!} e^{-\mu_i}$$

with N_i being the observed total number of counts in pixel i and μ_i being the total number of counts in the model. (The model has been renamed for better readability.)

The joint probability density function is

$$f_{\text{joint}} = \prod_i f(N_i, \mu_i).$$

Taking the logarithm and omitting terms that do not depend on the model μ gives the log-likelihood function

$$\log(L) = \sum_i N_i \log(\mu_i) - \mu_i.$$

Its maximum determines the parameters of the model that is given by $\mu = k \cdot N_{\text{low}} + c$ where k is the proportionality parameter and c the isotropic-background parameter. The optimization has been performed with the *iminuit* package based on CERN MINUIT (James & Roos 1975).

Bibliography

- [1] S. Funk. *Space- and Ground-Based Gamma-Ray Astrophysics*. arXiv:1508.05190 (2015).
- [2] M. S. Longair. *High Energy Astrophysics*. Cambridge University Press, Cambridge, 3rd edition (2011).
- [3] NASA. *Fermi Science Support Center*. <http://fermi.gsfc.nasa.gov/ssc/> (2016).
- [4] L. A. White, Symmetry Magazine. *Fermi's first five years*. <http://www.symmetrymagazine.org/article/august-2013/fermis-first-five-years> (2013).
- [5] M. Ackermann, A. Albert, W. B. Atwood et al. *The Spectrum and Morphology of the Fermi Bubbles*. arXiv:1407.7905v1 (2014).
- [6] NASA. *Radio Telescopes Capture Best-Ever Snapshot of Black Hole Jets (Centaurus A)*. <http://www.nasa-usa.de/topics/universe/features/radio-particle-jets.html> (2011).
- [7] G. Dobler, D. P. Finkbeiner, I. Cholis et al. *The Fermi Haze: A Gamma-ray Counterpart to the Microwave Background*. arXiv:0910.4583v2 (2010).
- [8] M. Su, T. Slatyer, D. P. Finkbeiner. *Giant Gamma-Ray Bubbles from Fermi-LAT: AGN Activity or Bipolar Galactic Wind?* arXiv:1005.5480v3 (2010).
- [9] Stanford University. *The Fermi LAT instrument*. <https://www-glast.stanford.edu/instrument.html> (2016).
- [10] M. G. F. Kirsch, U. G. Briel, D. Burrows et al. *Crab: the standard X-ray candle with all (modern) X-ray satellites*. arXiv:0508235 (2005).
- [11] G. Cowan. *Statistical Data Analysis*. Oxford University Press, Oxford (1998).
- [12] J. Höfer. *Analysis of an Excess Flux of Gamma Rays at 30 Degrees in Longitude in the Plane of the Milky Way Galaxy*. Bachelor's thesis at FAU Erlangen-Nuremberg

- (2016).
- [13] NASA. *HEALPix Introduction*. <http://healpix.jpl.nasa.gov/> (2016).
- [14] The *Fermi* collaboration. *The Fermi Galactic Center GeV Excess and Implications for Dark Matter* (Unpublished).
- [15] SLAC. *Fermi LAT Performance*. http://www.slac.stanford.edu/exp/glast/groups/canda/lat_Performance.htm (2016).
- [16] F. Acero, M. Ackermann, M. Ajello. *Development of the Model of Galactic Interstellar Emission for Standard Point-Source Analysis of Fermi Large Area Telescope Data*. *ApJS* 223:26 (2016).

Acknowledgements

I want to thank everybody who helped me with my bachelor's thesis during the last three months, especially:

- Prof. Dr. Stefan Funk for giving this interesting topic to me.
- Prof. Dr. Christopher van Eldik for being the second corrector.
- My supervisor Dmitry Malyshev. You are really a great supervisor with lots of good ideas! It is fun working with you.
- My temporary supervisor Tobias Jogler for introducing me to the topic and always telling good stories.
- Judith Höfer for answering a lot of questions. Your bachelor's thesis [12] was great help. Thanks also for the detailed proofreading!
- Johannes Schäfer for his great proofreading.
- And of course thanks to the best office **108a**, for moral support, help, fun and endless supply with cookies ☺☺☺.

Erklärung

Hiermit bestätige ich, dass ich diese Arbeit selbstständig und nur unter Verwendung der angegebenen Hilfsmittel angefertigt habe. Erlangen, den 29.11.2016